OPEN ACCESS



NuSTAR Observes Two Bulgeless Galaxies: No Hard X-Ray AGN Detected in NGC 4178 or J0851+3926

Ryan W. Pfeifle 1,2,11 , Shobita Satyapal , Claudio Ricci 3,4,5 , Nathan J. Secrest , Mario Gliozzi , Thomas Bohn , Cabriela Canalizo , and Michael A. Reefe 3,9,10,12

1 X-Ray Astrophysics Laboratory, NASA Goddard Space Flight Center, Code 662, Greenbelt, MD 20771, USA; ryan.w.pfeifle@nasa.gov

2 Oak Ridge Associated Universities, NASA NPP Program, Oak Ridge, TN 37831, USA

3 Department of Physics and Astronomy, George Mason University, 4400 University prive, MSN 3F3, Fairfax, VA 22030, USA

4 Núcleo de Astronomía de la Facultad de Ingeniería, Universidad Diego Portales, Av. Ejército Libertador 441, Santiago, Chile

5 Kavli Institute for Astronomy and Astrophysics, Peking University, Beijing 100871, People's Republic of China

6 U.S. Naval Observatory, 3450 Massachusetts Avenue NW, Washington, DC 20392, USA

7 Hiroshima Astrophysical Science Center, Hiroshima University, 1-3-1 Kagamiyama, Higashi-Hiroshima, Hiroshima 739-8526, Japan

8 University of California, Riverside, Department of Physics & Astronomy, 900 University Avenue, Riverside, CA 92521, USA

9 Department of Physics, Massachusetts Institute of Technology, Cambridge, MA 02139, USA

Abstract

Received 2022 October 20; revised 2022 November 28; accepted 2022 November 30; published 2023 January 31

The discovery over the last several decades of low- and moderate-luminosity active galactic nuclei (AGNs) in diskdominated galaxies—which show no "classical" bulges—suggests that secular mechanisms represent an important growth pathway for supermassive black holes in these systems. We present new follow-up NuSTAR observations of the optically elusive AGNs in two bulgeless galaxies, NGC 4178 and J0851+3926. Galaxy NGC 4178 was originally reported as hosting an AGN based on the detection of [Ne V] mid-infrared emission detected by Spitzer, and based on Chandra X-ray imaging, it has since been argued to host either a heavily obscured AGN or a supernova remnant. Galaxy J0851+3926 was originally identified as an AGN based on its Wide-Field Infrared Survey Explorer mid-IR colors, and follow-up near-infrared spectroscopy previously revealed a hidden broad-line region, offering compelling evidence for an optically elusive AGN. Neither AGN is detected within the new NuSTAR imaging, and we derive upper limits on the hard X-ray $10-24\,\mathrm{keV}$ fluxes of $<7.41\times10^{-14}$ and $<9.40 \times 10^{-14} \text{ erg cm}^{-2} \text{ s}^{-1}$ for the AGNs in NGC 4178 and J0851+3926, respectively. If these nondetections are due to large absorbing columns along the line of sight, the nondetections in NGC 4178 and J0851+3926 could be explained with column densities of $\log(N_{\rm H}/{\rm cm}^2) > 24.2$ and 24.1, respectively. The nature of the nuclear activity in NGC 4178 remains inconclusive; it is plausible that the [Ne V] traces a period of higher activity in the past, but that the AGN is relatively quiescent now. The nondetection in J0851+3926 and multiwavelength properties are consistent with the AGN being heavily obscured.

Unified Astronomy Thesaurus concepts: Active galactic nuclei (16); AGN host galaxies (2017); Low-luminosity active galactic nuclei (2033)

1. Introduction

The well-known correlation between the black hole mass and the host galaxy's stellar velocity dispersion (e.g., Magorrian et al. 1998; Gebhardt et al. 2000; Gültekin et al. 2009b; McConnell & Ma 2013) launched a long-standing view that black hole growth and the buildup of galaxy bulges go hand in hand, perhaps as interactions fuel the central supermassive black hole (SMBH) and grow the bulge, and feedback from the active galactic nucleus (AGN) regulates the surrounding star formation in the host galaxy (e.g., Toomre 1977; Barnes 1992; Silk & Rees 1998; Kauffmann & Haehnelt 2000; Hopkins et al. 2012). The connection between black hole growth and galaxy bulges was further intimated by the fact that until recently, virtually all currently known actively accreting black holes—i.e., AGNs—in the local universe were found in galaxies with

Original content from this work may be used under the terms of the Creative Commons Attribution 4.0 licence. Any further distribution of this work must maintain attribution to the author(s) and the title of the work, journal citation and DOI.

prominent bulges (e.g., Ho et al. 1997; Kauffmann et al. 2003). In recent years, however, it has become clear that many moderate-luminosity ($L_{0.5-8\text{keV}} = 10^{42} - 10^{44} \text{ erg s}^{-1}$) AGNs are found in disk-dominated galaxies with no signs of interactions (e.g., Kocevski et al. 2012; Simmons et al. 2012). Although some mergers can regrow or leave large-scale disks (Springel & Hernquist 2005; Hopkins et al. 2009), and it may be possible to build a "classical" bulge without mergers (Bell et al. 2017), it is extremely likely that the vast majority of disk-dominated galaxies in the local universe have evolved largely independently from mergers since $z \approx 2$ (Martig et al. 2012). The discovery of significant AGN activity in disk galaxies therefore stresses the importance of secular pathways in black hole growth. Surprisingly, in the few disk-dominated galaxies with optically identified AGNs, the black hole mass is found to correlate with the total stellar mass of the disk (e.g., Cisternas et al. 2011; Simmons et al. 2017). Since the bulge carries the imprint of the merger history of a galaxy, this suggests that SMBH and galaxy coevolution takes place largely independently from mergers. However, most past studies are based on optical spectroscopic observations, which can be severely limited in the study of bulgeless galaxies. It is well known that the infrared-to-blue luminosity ratio observed in galaxies

NASA Postdoctoral Program Fellow.

¹² National Science Foundation, Graduate Research Fellow.

increases along the Hubble sequence, implying that late-type galaxies are extremely dusty (e.g., de Jong et al. 1984). In addition, the optical emission lines used to identify AGNs get increasingly diluted by star formation in the host as the bulge-to-disk ratio decreases (e.g., Trump et al. 2015). In an effort to study obscured AGN growth in bulgeless galaxies, we focus in this work on NGC 4178 and SDSS J085153.64+392611.76 (hereafter J0851+3926), both of which have been reported to host optically elusive, heavily obscured AGNs.

The bulgeless spiral galaxy NGC 4178 resides at a distance of 16.2 Mpc away (Kent et al. 2008) in the Virgo Cluster. Satyapal et al. (2009) first reported on the presence of an AGN in NGC 4178 based on the detection of a high-ionization [Ne V] $\lambda 14.3 \,\mu m$ emission line—a reliable tracer of AGN activity (Abel & Satyapal 2008) in the mid-infrared (mid-IR)—using the Spitzer Space Telescope. Given that the optical emission shows no sign of an AGN and instead is consistent with an HII star-forming region (e.g., Secrest et al. 2012), the detection of the [Ne V] emission line suggested that NGC 4178 in fact hosted an optically elusive AGN. Follow-up Chandra observations presented in Secrest et al. (2012) revealed a weak (5.3σ) and predominantly soft X-ray point source coincident with the nucleus of the galaxy. Secrest et al. (2012) concluded that the X-ray source properties were consistent with a heavily obscured AGN with an absorbing column density of $N_{\rm H}=5 \times 10^{24} {\rm cm}^{-2}$, a covering factor of C=0.99, and a photon index of $\Gamma=2.3^{+0.6}_{-0.5}$. Using (1) the [Ne V] emission line flux to estimate the bolometric luminosity, as well as (2) an archival Very Large Array image to utilize the fundamental plane of black hole accretion (e.g., Gültekin et al. 2009a), Secrest et al. (2012) estimated that the AGN is powered by an $\sim 7 \times 10^4 - 2 \times 10^5 \, M_{\odot}$ intermediate-mass black hole. However, the AGN interpretation has recently been called into question by Hebbar et al. (2019), who instead claimed that the X-ray emission is better fit by a hot plasma model and that the X-ray emission is likely due to a supernova remnant. Graham et al. (2019), too, recently questioned the AGN interpretation, suggesting that perhaps the [Ne V] emission traces a period of previous activity but that the AGN is relatively quiescent now.

J0851+3926 is a bulgeless spiral galaxy at z = 0.1296originally selected by Satyapal et al. (2014) based on its Wide-Field Infrared Survey Explorer (WISE) mid-IR colors; J0851 +3926 satisfied the stringent three-band mid-IR AGN color cut defined by Jarrett et al. (2011), suggestive of a powerful, dustobscured AGN. It was selected again in Bohn et al. (2020) in an effort to measure black hole masses in optically elusive AGNs in bulgeless galaxies. While the Baldwin-Phillips-Terlevich (Baldwin et al. 1981) optical spectroscopic line ratios are consistent with a composite galaxy (Bohn et al. 2020) which is commonly assumed to arise from a mixture of AGN and star formation-driven emission, based on the criteria laid out in Kewley et al. (2001, 2006) and Kauffmann et al. (2003) —shocks can also give rise to similar emission line ratios, leading to an ambiguous optical classification (e.g., Allen et al. 2008; Rich et al. 2011, 2014). Coupled with the lack of Balmer emission lines in the optical band, there is no definitive evidence in the optical for an AGN (Satyapal et al. 2014; Bohn et al. 2020). As a part of their elusive AGN campaign, Bohn et al. (2020) published near-infrared spectra obtained from the Near-Infrared Echellette Spectrometer (NIRES) and Near-Infrared Spectrometer (NIRSPEC) on Keck for J0851+3926

Table 1
NuSTAR Observations

Name	ObsID	FPM	Exp.	Net Exp.
(1)	(2)	(3)	(ks) (4)	(ks) (5)
NGC 4178	60601013002	A	58.3	54.0
	60601013002	В	58.3	53.4
J0851+3926	60501025002	A	61.4	52.9
	60501025002	В	61.4	52.5

Note. Relevant information for NuSTAR data observations. Columns (1)–(3): target name, observation ID, and camera. Columns (4) and (5): total raw exposure time and net exposure time after processing the data.

and reported the detection of a broad $(1489 \pm 184 \,\mathrm{km \, s}^{-1})$ in NIRSPEC, $1363 \pm 31 \text{ km s}^{-1}$ in NIRES) Pa α emission line in both observations. After ruling out the possibility that the broad emission line is due to outflows or a supernova, the authors attributed the broad Pa α emission to an optically elusive AGN. An X-ray AGN was not detected in the Chandra imaging, but the 3σ upper limit on the 2–10 keV flux implied a column density of $log(N_H/cm^2) \ge 24.43$ (Bohn et al. 2020) based on the relationship between the observed 2–10 keV and 12 μ m emission derived in Pfeifle et al. (2022). This column density is consistent with the lack of broad optical emission lines and the derived level of extinction $(E_{\text{H}\alpha}(B-V \geqslant 1.40))$; Bohn et al. 2020). Virial mass measurements using the broad Pa α emission yielded an (extinction-corrected) mass of $\log(M/M_{\odot})$ = 6.78 ± 0.50 for the optically elusive, heavily obscured AGN (Bohn et al. 2020).

Here we report on new NuSTAR observations of NGC 4178 and J0851+3926 that were carried out with the goal of understanding whether AGNs are present in these galaxies and to provide constraints on the obscuring columns. We organize this work as follows. In Section 2, we describe the observations and processing of the NuSTAR and Chandra observations, and in Section 3, we describe our data analysis. In Section 4, we describe our results. In Section 5, we discuss our work in the context of our previous work and the literature, and in Section 6, we present our conclusions. Throughout this paper, we adopt the following cosmology: $H_0 = 70 \text{ km s}^{-1} \text{ Mpc}^{-1}$, $\Omega_M = 0.3$, and $\Omega_\Lambda = 0.7$.

2. Observations and Data Processing

2.1. NuSTAR Observations

The NuSTAR observations for NGC 4178 (58.3 ks; ObsID 60601013002; PI: Satyapal) and J0851+3926 (61.4 ks; ObsID 60501025002; PI: Satyapal) were conducted on 2020 June 25 and 2020 May 8, respectively (see Table 1). Reprocessing of the data was performed using the NuSTAR Data Analysis Software (NUSTARDAS; Perri et al. 2021)¹³ v0.4.7 package available in HEASOFT v6.27 (Nasa High Energy Astrophysics Science Archive Research Center 2014) along with the latest CALDB and clock correction file at that time. The NUPIPELINE script was used to conduct stage 1 and 2 reprocessing, and we used the background light curves for each observation to inform our choices for the South Atlantic Anomaly (SAA) calculation. For both observations, we used SAA algorithm 1; we chose the "Optimized" and "Strict" calculation modes for

¹³ https://heasarc.gsfc.nasa.gov/docs/nustar/analysis/

NGC 4178 and J0851+3926, respectively; and we did not employ the "tentacle" option¹⁴ in either case, since a stable background light curve was achieved using the aforementioned algorithm settings. Energy-filtered event files were created using DMCOPY in the Chandra Interactive Analysis of Observations (CIAO) software package (Fruscione et al. 2006).¹⁵ The NUPRODUCTS script was used to extract the stage 3 spectroscopic data products using the source and background regions described in Section 3. Due to the low number of counts, extracted spectra were grouped by 1 count bin⁻¹ using the HEASOFT GRPPHA command in order to use Cash statistics (Cash 1979) during fitting.

2.2. Chandra Observation

In addition to the NuSTAR observations of NGC 4178 and J0851+3926, we also retrieved their archival Chandra observations. NGC 4178 was observed for 40 ks (ObsID 12748) on 2011 February 19 and examined in Secrest et al. (2012), Hebbar et al. (2019), and, most recently, Graham et al. (2019). J0851+3926 was observed for 20 ks (ObsID 22584) and examined in Bohn et al. (2020). These observations were reprocessed using CIAO v.4.12 and CALDB v4.9.1 using the CHANDRA_REPRO script. Energy-filtered images were again created using DMCOPY within CIAO. Spectra were extracted using the SPECEXTRACT script and, as in the case of the NuSTAR data, grouped by 1 count bin⁻¹.

3. Analysis

3.1. NuSTAR Source Detection and Photometry

Neither NGC 4178 nor J0851+3926 host an obvious hard X-ray point source upon visual inspection. To search the NuSTAR FPMA and FPMB images for potential sources, we employed WAVDETECT from CIAO on the observed frame 3–8 keV band, as well as the more traditional 3–10, 10–24, and 3-24 keV NuSTAR bands for both galaxies. WAVDETECT found no sources in either FPMA or FPMB at the location of J0851+3926. One source is detected by WAVDETECT in the 3-8, 3-10, and 3-24 keV FPMA images of NGC 4178, but the source is not found in the FPMA 10-24 keV band, nor is it detected in FPMB in any band. Because the detections in the 3-10 and 3-24 keV bands are due largely to the detection of a source in the 3–8 keV band, and because the WAVDETECT 3–10 keV region was not well centered on the source centroid, we used the 3-8 keV band for the source aperture placement for NGC 4178.

Since WAVDETECT did not find any source at the location of J0851+3926, we instead used an aperture of 45" in radius centered on the Sloan Digital Sky Survey (SDSS) optical position of the galaxy to extract counts from both FPMA and FPMB. An annular region with an inner and outer radius of 90" and 150", respectively, was also centered on the galaxy's position and used to sample the background for both cameras.

The placement of apertures for source and background extraction for NGC 4178 required more care. Although the average astrometry accuracy of NuSTAR's pointing is often

quoted as $\sim 8''$ for bright sources (Harrison et al. 2013), the average positional accuracy of NuSTAR can range from $\sim 14''$ for the brightest sources to $\sim 22''$ for the weakest sources (see, e.g., Figure 4 and Section 3.1 in Lansbury et al. 2017). The source identified by WAVDETECT in the FPMA 3-8 keV band located at $\alpha = 12^{\rm h}12^{\rm m}44.86$, $\delta = +10^{\circ}51^{\rm m}20.71$ (in FPMA) lies ~ 40.1 from the putative AGN's position ($\alpha =$ $12^{\rm h}12^{\rm m}46^{\rm s}32$, $\delta = 10^{\rm h}51^{\rm m}54^{\rm s}61$, derived from Chandra X-ray imaging; Secrest et al. 2012). Given the average range of offsets observed by Lansbury et al. (2017), if this source is indeed the AGN, its positional offset from the reported Chandra position would be exceptionally large. On the other hand, the source is offset by only ~8."8 from the ultraluminous X-ray source (ULX), located at $\alpha = 12^{h}12^{m}44.51$, $\delta = 10^{\circ}51^{m}13.64$ within NGC 4178 (Secrest et al. 2012), suggesting that the source detected by NuSTAR is in fact the ULX. If we assume that the positional offset between the NuSTAR and Chandra positions is due strictly to the positional accuracy of NuSTAR, the source's positional offset from the AGN is \sim 49", exactly that found for the ULX (Secrest et al. 2012). We therefore conclude that the source detected by NuSTAR is more likely the ULX.

Due to the angular resolution of NuSTAR (\sim 18" FWHM; Harrison et al. 2013) and the angular separation between the ULX and putative AGN (\sim 49"), the source apertures had to be chosen carefully so as to avoid (as much as possible) contamination at the position of the putative AGN by the nearby, brighter ULX. This is particularly important in the calculation of upper limits in the event of a nondetection for the AGN. To better understand the radial extent of the ULX, we placed a series of equally spaced concentric annuli with radii extending from 0" to 80" and measured the number of counts within each annulus. We show the radial profile for the ULX along with the NuSTAR 3-10 keV image with the annuli overlaid in Figure 1. The surface brightness decreases steadily from 0'' out to $\sim 28''$ from the ULX, beyond which the surface brightness becomes fairly constant. We can therefore justify the choice of a 30" radius aperture centered on the position of the ULX as determined by WAVDETECT. At the position of the reported AGN, we use a slightly smaller radius aperture of 18" (so that it does not intersect the extraction region for the ULX) centered on the expected position of the AGN based on the NuSTAR positional offset. 16 Because the source was not detected in FPMB, we loaded the FPMA regions in DS9 on top of the FPMB image and used the centroid feature to center the ULX aperture to try and account for the positional offset between FPMA and FPMB, which we found to be \sim 4."6. Based on this shift, we then shifted the AGN aperture to its expected FPMB position. As for the background regions, in order to avoid sampling from areas of the image that overlap with NGC 4178 or other potential sources in the field of view, we used a set of four 60" radius apertures spaced around NGC 4178.

For the Chandra observations of NGC 4178 and J0851 +3926, we used apertures (1".5 in radius) identical to those used in Secrest et al. (2012) and Bohn et al. (2020), respectively. A circular aperture of 20" in radius was used to

 $[\]overline{^{14}}$ See page 35 of the NUSTARDAS data analysis software guide for a description of the "tentacle" option.

¹⁵ A note of caution: for the filtered exposure time, DMEXTRACT searches the header for the keyword "DTCOR," but NuSTAR observations use the keyword "DTIME." To retrieve the correct exposure time alongside the source counts, one needs to modify the event file header to include "DTCOR." Otherwise, DMEXTRACT assumes that the exposure time is equal to the live time.

¹⁶ To account for this offset, we loaded into DS9 the WAVDETECT-determined NuSTAR aperture (listed in Table 2), as well as the Chandra apertures for the AGN and ULX positions given by Secrest et al. (2012). We then manually shifted the two apertures from Secrest et al. (2012) until the Chandra and NuSTAR ULX apertures were cospatial and then recorded the expected position of the AGN within the NuSTAR image.

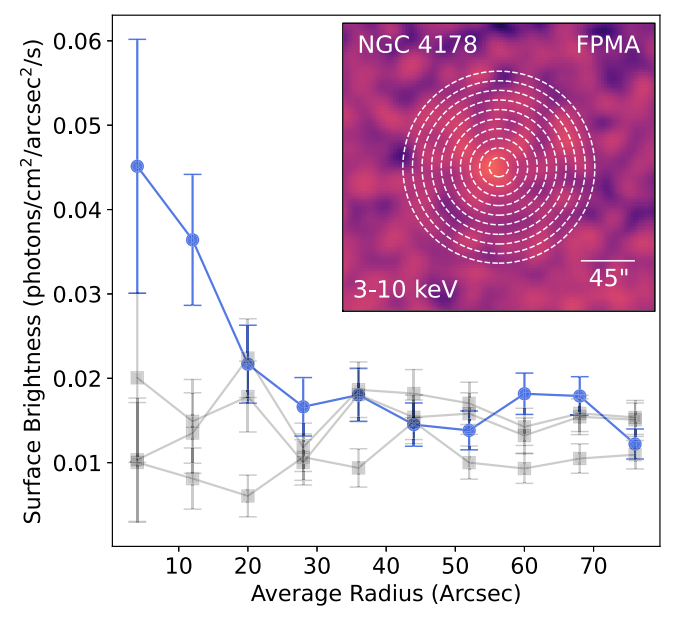


Figure 1. Surface brightness as a function of radial distance from the ULX in NGC 4178. The source in the NuSTAR FPMA 3–10 keV band is shown in the top right corner, where the data are smoothed using a 3 pixel Gaussian kernel and displayed with a perceptually uniform color map. Concentric white dashed circles indicate the annuli from which counts were extracted to construct the radial profile of the ULX. The radial profile is shown using the blue points connected with a line; error bars represent the standard error. The surface brightness of the source decreases from the source center out to $\sim 28''$, after which the surface brightness varies little with radial distance. Radial surface brightness profiles for three nearby, background-dominated areas are shown in gray for comparison.

sample the background in a source-free region of the ACIS-S detector for each observation.

DMEXTRACT from CIAO was used to extract source and background counts using the regions described above. We required a significance threshold of 3σ for a source to be considered detected. For sources with greater than 20 counts and a 3σ detection in a particular energy band, we assume that the photon count distribution is Gaussian and compute the error on the counts in that band as \sqrt{N} , where N is the number of counts. For nondetections ($<3\sigma$), we instead compute the 3σ (99.7% confidence level) upper limits for the net source counts using the gross measured counts in the source and background regions following the Bayesian method of Kraft et al. (1991). Additionally, due to either weak or undetected sources, we compute the binomial no-source probability $(P_{\rm B})$ for each energy band (see Equation (1) in Section 3 of Lansbury et al. 2014). We required a source to meet a threshold of $(P_{\rm B}) > 0.002$ in order to be considered statistically significant, as opposed to being the result of a spurious background fluctuation.

3.2. Flux Calculations

For the AGNs in NGC 4178 and J0851+3926, we used the Chandra PIMMS toolkit to calculate upper limits for the observed fluxes in each of the 3–24, 3–10, and 10–24 keV bands (as well as the 2–10 keV band for direct comparison to previous work with Chandra) based on the count rates derived for each position. PIMMS assumes that the input is the total two-camera (FPMA + FPMB) count rate and is retrieved from an aperture enclosing 50% of the enclosed energy fraction (EEF), which corresponds to an aperture size of $\sim\!\!30''$ for NuSTAR

(Harrison et al. 2013). During this step, for each band, we combined the count rate upper limits derived from FPMA and FPMB and, where appropriate, applied a scale factor to correct the count rates to the 50% EEF. We then provided these count rates to PIMMS. We assumed a power-law model with photon index $\Gamma=1.8$ (Mushotzky et al. 1993; Ricci et al. 2017) for J0851+3926, while we calculated two fluxes per energy band for NGC 4178, one assuming $\Gamma=2.6$ (the unobscured AGN case from Secrest et al. 2012) and one assuming $\Gamma=2.3$ (the obscured case from Secrest et al. 2012). We also took into account Galactic absorption along the line of sight, obtained from the Swift Galactic $N_{\rm H}$ calculator (Willingale et al. 2013). ¹⁸

3.3. Indirect Estimates of AGN Column Densities

Without sufficient counts to enable direct spectral fitting, we instead estimated a lower limit on the column density along the line of sight to the AGNs in both galaxies using (1) the ratio between the observed upper limit on the 10–24 keV NuSTAR flux and the expected, intrinsic 10–24 keV flux and (2) sets of attenuation curves (see, e.g., Figure 1 in Ricci et al. 2015) generated with XSPEC (Arnaud 1996). First, we established a model in XSPEC consisting of a primary power law, photoelectric absorption (TBABS) and Compton scattering (CABS), and a component to account for reprocessed radiation (BORUS; Balokovic et al. 2018), as well as a component for Thomson-scattered X-ray radiation (F*CUFFPL), expressed as

 $(F \times CUTOFFPL) + (TBABS \times CABS \times CUTOFFPL) + BORUS,$

which we stepped through a range of column densities 22 ≤ $\log(N_{\rm H}/{\rm cm}^{-2}) \leq 25.4$ in increments of $\Delta \log(N_{\rm H}/{\rm cm}^{-2}) =$ 0.2. We assumed a power law with a photon index of $\Gamma = 1.8$ (e.g., Mushotzky et al. 1993; Ricci et al. 2017) for J0851 +3926, and we used two different photon index choices (Γ = 2.6 and 2.3) for NGC 4178, as we did in the PIMMS flux calculations. Furthermore, we assumed a scattering fraction of 0.5% (f = 0.005, similar to the scattering fractions found for obscured Swift/BAT AGNs, e.g., Ricci et al. 2017, and close to what might be expected in the case of heavily buried AGNs, e.g., Ueda et al. 2007), and we tested this model using two different covering factors (C): 0.5 and 0.99. These choices reflect two scenarios: one in which the AGNs host a more "standard" obscuring torus (C = 0.5) and one in which the AGN is heavily buried with a high covering factor (C = 0.99). For each step through $\log(N_{\rm H}/{\rm cm}^{-2})$ space, we recorded the 2-10 and 10-24 keV fluxes. Using these fluxes, we then built two attenuation curves, one for C = 0.5 and one for C = 0.99, for the hard X-ray 10-24 keV emission of both galaxies, where the curves are normalized to the "intrinsic" 10-24 keV flux measured when $\log(N_{\rm H}/{\rm cm}^{-2}) = 22.0$.

We then computed the expected intrinsic $10-24\,\mathrm{keV}$ fluxes of each AGN. For J0851+3926, this involved first computing the expected 2–10 keV flux based on the WISE $12\,\mu\mathrm{m}$ fluxes (using the relation from Asmus et al. 2015) and then converting the intrinsic 2–10 keV flux to the intrinsic $10-24\,\mathrm{keV}$ flux using XSPEC, again assuming $\Gamma=1.8$. For NGC 4178, we instead adopted the 2–10 keV fluxes found by Secrest et al. (2012) using

 $[\]overline{^{17}}$ Thus, the count rates for NGC 4178 were scaled up to 50%, and the rates for J0851+3926 were scaled down to 50%.

¹⁸ https://www.swift.ac.uk/analysis/nhtot/

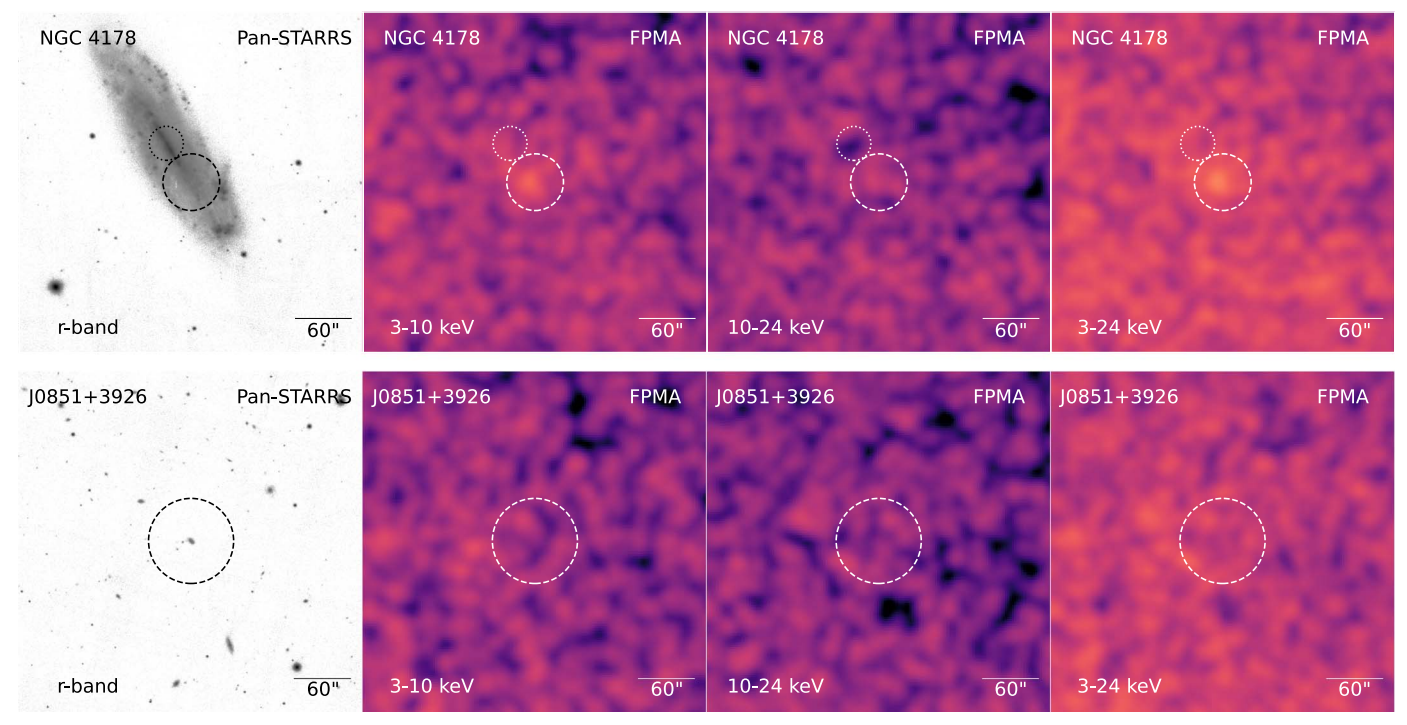


Figure 2. Pan-STARRS r-band and NuSTAR FPMA imaging for NGC 4178 (top) and J0851+3926 (bottom). Left to right: Pan-STARRS r band, NuSTAR FPMA 3–10, 10–24, and 3–24 keV bands. The X-ray images are smoothed using a 3 pixel Gaussian kernel and displayed with the perceptually uniform sequential color map "magma" in MATPLOTLIB. Top: dashed 30" radius circles represent the extraction region for the ULX, while dotted 18" radius circles represent the AGN extraction region; these circles are offset by \sim 49" from one another. Bottom: dashed 45" radius circles represent the AGN extraction region.

Chandra: $6.9 \times 10^{38}~{\rm erg~cm^{-2}~s^{-1}}$ for the unobscured case (which used a power-law model with $\Gamma=2.6$) and $8.6 \times 10^{39}~{\rm erg~cm^{-2}~s^{-1}}$ in the obscured case (which used a power-law model with $\Gamma=2.3$).

Finally, we took the ratio between the observed upper limit on the 10-24 keV NuSTAR flux (Table 3) and the expected intrinsic 10-24 keV flux and used the attenuation curves to obtain lower limits on the column density along the line of sight. We thus obtain for each galaxy two lower limits on the column density, one assuming C = 0.5 and one assuming C = 0.99. Both lower limits are quoted in this work for J0851 +3926. For NGC 4178, however, the intrinsic X-ray fluxes used in these calculations were model-specific; the intrinsic flux for the obscured case was derived assuming $\Gamma = 2.3$ and a high covering factor (C = 0.99), while the unobscured case assumed $\Gamma = 2.6$ and had no requirements for the covering factor. To maintain consistency, for the unobscured case $(\Gamma = 2.6)$, we quote only the $N_{\rm H}$ lower limit derived using C = 0.5, and for the obscured case ($\Gamma = 2.3$), we quote only the $N_{\rm H}$ lower limit derived using C = 0.99.

4. Results

We show the NuSTAR 3–10, 10–24, and 3–24 keV images along with Pan-STARRS *r*-band images of NGC 4178 and J0851+3926 in Figure 2. Neither of the reported AGNs in NGC 4178 and J0851+3926 are detected in any NuSTAR energy band, so we instead calculated the upper limits on the counts and fluxes for each AGN candidate (as outlined in Section 3). The ULX in NGC 4178 was significantly detected in the 3–10 and 3–24 keV images. We report aperture positions and count statistics in Table 2 and X-ray fluxes of the AGNs in Table 3. In the case of NGC 4178, the nondetection suggests that there is no X-ray-emitting AGN with an observed flux in

excess of $7.41\times 10^{-14}~\rm erg~cm^{-2}~s^{-1}$ in the 10– $24~\rm keV$ band (assuming $\Gamma=2.3$). For J0851+3926, the nondetection suggests that there is no X-ray-emitting AGN with an observed flux in excess of $9.40\times 10^{-14}~\rm erg~cm^{-2}~s^{-1}~(\Gamma=1.8)$ in the 10– $24~\rm keV$ band. To offer a direct comparison to previous work with Chandra, we also derived the 2–10 keV flux upper limits for each system using the flux in the NuSTAR 3–10 keV band; there are no X-ray-emitting AGNs with observed 2–10 keV fluxes in excess of $7.36\times 10^{-14}~\rm erg~cm^{-2}~s^{-1}$ in the case of NGC 4178 ($\Gamma=2.3$) and $4.84\times 10^{-14}~\rm erg~cm^{-2}~s^{-1}$ in the case of NGC 4178 ($\Gamma=2.3$) and $4.84\times 10^{-14}~\rm erg~cm^{-2}~s^{-1}$ ($\Gamma=1.8$) in the case of J0851+3926. These 2–10 keV flux upper limits are consistent with the previous upper limits established using Chandra (Secrest et al. 2012; Bohn et al. 2020).

We also recalculated the 2–10 keV upper limits on the counts and flux for J0851+3926 using the archival Chandra imaging and used the appropriate Bayesian approach mentioned in Section 3. We found the upper limit on the counts to be <8 counts in the 0.3–8 keV band, <8 counts in the 0.3–2 keV band, and <6 counts in the 2–8 keV band based on the Chandra imaging. These counts in turn yield flux upper limits of <5.30 × 10^{-15} , <4.14 × 10^{-15} , and <5.51 × 10^{-15} erg cm⁻² s⁻¹ in the 0.3–8, 0.3–2, and 2–8 keV Chandra bands, respectively. Using the 2–8 keV flux upper limit, we found the 2–10 keV flux upper limit to be 6.55 × 10^{-15} erg cm⁻² s⁻¹. These flux upper limits supersede those calculated in Bohn et al. (2020).

In the absence of spectra, we have inferred lower limits to the column densities required for nondetections in the NuSTAR energy bands using the flux ratio calculations described in Section 3; we report these column densities in Table 3. In order to remain undetected by NuSTAR, the central source in J0851 +3926 would need to be obscured by $\log(N_{\rm H}/{\rm cm}^2) > 24.1$, assuming a covering factor of C = 0.5, or $\log(N_{\rm H}/{\rm cm}^2) > 24.3$, assuming C = 0.99. If NGC 4178 hosts a heavily obscured

Table 2
NuSTAR Photometry

System	FPM	α	δ	Net Counts		
(1)	(2)	(3)	(4)	3–24 keV (5)	3–10 keV (6)	10–24 keV (7)
NGC 4178, ULX	A	12 ^h 12 ^m 44 ^s 864	+10°51 ^m 20 ^s 709	47.0 ± 12.9	38.3 ± 10.2	<28.6
	В	12 ^h 12 ^m 44.588	$+10^{\circ}51^{m}18:054$	38.8 ± 12.5	29.7 ± 9.8	<28.8
NGC 4178, AGN	A	12 ^h 12 ^m 46 ^s 663	$+10^{\circ}52^{m}01\stackrel{s}{.}711$	<21.2	<21.5	<10.3
	В	12h12m46 s 394	$+10^{\circ}51^{m}58 \stackrel{s}{.} 366$	<29.7	<23.8	<16.0
J0851+3926	A	08 ^h 51 ^m 53 ^s .743	$+39^{\circ}26^{m}11 \stackrel{s}{.} 526$	<62.8	<40.8	<40.2
	В			<41.0	<33.5	<29.0

Note. NuSTAR photometry for the 3–24, 3–10, and 10–24 keV energy bands. Columns (1) and (2): system name and FPM. Columns (3) and (4): R.A. and decl. of the source apertures. Columns (5)–(7): net source counts for the 3–24, 3–10, and 10–24 keV energy bands (see Section 3).

AGN, as posited by Secrest et al. (2012), it would need to be obscured by $\log(N_{\rm H}/{\rm cm}^2) > 24.2$ (assuming $\Gamma = 2.3$ and C = 0.99) to remain undetected by NuSTAR in the 10–24 keV band. If NGC 4178 instead hosts an unobscured AGN ($\Gamma = 2.6$; Secrest et al. 2012), its intrinsic flux is below the detection limit of the NuSTAR observation.¹⁹

5. Discussion

5.1. NGC 4178

The lack of a hard X-ray point source in NGC 4178 offers little constraint on the presence or absence of an AGN. Based upon our analysis, if an X-ray-emitting AGN exists in the nucleus of NGC 4178, it is either a Compton-thick AGN with $\log(N_{\rm H}/{\rm cm}^{-2}) > 24.2$ —in general agreement with the column density estimated by Secrest et al. (2012) for their heavily obscured AGN case—or a low-luminosity AGN (LLAGN) with column density $\log(N_{\rm H}/{\rm cm}^{-2}) \le 22$ and a flux level below the detection limit of NuSTAR.

Recently, Hebbar et al. (2019) examined the Chandra spectra of the nuclear source in NGC 4178 and found that the spectrum is poorly fit by an absorbed power-law model (PCFAB-S*PEGPWRLW)—which would arise in the case of an obscured AGN—but is better fit and more resembles emission from a supernova remnant, modeled via a hot plasma model (TBABS*VAPEC in XSPEC). This result suggests that the X-ray emission is not dominated by an AGN, either because there is no AGN or because it is too obscured. To compare the bestfitting model from Hebbar et al. (2019) to the nondetections in the NuSTAR imaging, we refit the Chandra 0.3–8 keV spectra using the TBABS*VAPEC model and froze all parameters to the best-fit values in Table 2 from Hebbar et al. (2019) except for the normalization, which was left free to vary. We then fit the model to recover the approximate normalization. Using this model, we found that the absorbed hot plasma model returns²⁰ an observed 2–10 keV X-ray flux of $2.0^{+0.3}_{-0.4}\times10^{-15}$ erg cm⁻² s⁻¹ and a 3–10 keV observed flux of $6.4^{+1.0}_{-1.0}\times10^{-16}$ erg cm⁻² s⁻¹. These fluxes are a magnitude or more lower than the upper limits derived for any AGN in NGC 4178, placing such a source well below the detection threshold of the NuSTAR imaging. At this expected flux level, a nondetection is consistent with the picture that the nuclear X-ray flux is dominated by a supernova remnant, but unfortunately, the NuSTAR data are inconclusive in this respect and cannot provide strong evidence for or against either scenario.

In an effort to uncover any trace of AGN activity in NGC 4178, we examined the SDSS optical spectra to search for optical coronal lines that might have arisen due to an AGN; no optical coronal lines are found in the optical spectra. Similarly, we have examined the WISE mid-IR colors from the AllWISE point-source catalog (Wright et al. 2019), as well as the mid-IR colors derived from the NEOWISE reactivation database (NEOWISE Team 2020); at no point in time do we find any evidence for a mid-IR AGN based on the commonly employed selection criteria of Jarrett et al. (2011) and Stern et al. (2012). We should note that while NGC 4178 does not manifest as an AGN in the mid-IR, its mid-IR colors are not unlike those of other [Ne V]-emitting AGNs in the local universe; Figure 3 shows that NGC 4178 (blue diamond) occupies the same mid-IR color space as that of other, local redshift, [Ne V]-emitting AGNs (open circles) that fall outside of the selection criteria from Jarrett et al. (2011) and Stern et al. (2012), so the lack of a mid-IR AGN should not immediately discount an AGN scenario. However, given the ambiguity surrounding the nature of the nuclear X-ray source and the lack of optical and mid-IR signatures, we cannot provide any definitive evidence that supports or refutes either scenario proposed by Secrest et al. (2012) and Hebbar et al. (2019).

Interestingly, this situation is reminiscent of NGC 3486—as one example—in that a high-excitation line attributed to AGN activity was reported (O VI in NGC 3486 and Ne V in NGC 4178; Satyapal et al. 2009; Annuar et al. 2020), and an AGN was reported based on soft X-ray emission TMM-Newton ($L_{2-10\text{keV}} = 1.1 \times 10^{39}$ erg s⁻¹ in NGC 3486; Cappi et al. 2006) or Chandra ($L_{2-10\text{keV}} = 7.9 \times 10^{38}$ erg s⁻¹ in NGC 4178; Secrest et al. 2012) but was not detected in the NuSTAR imaging (Annuar et al. 2020, and this work). The major difference in this comparison is that NGC 3486 is detected as a Type II AGN in the optical, whereas NGC 4178 presents as an H II star-forming region.

Perhaps the most plausible explanation for the lack of a hard X-ray or optical AGN in NGC 4178 is that the [Ne V] detection is a light echo tracing AGN activity in the past, as has recently been suggested by Graham et al. (2019). The Spitzer SH slit subtends a large fraction of the nuclear region of NGC 4178 (but it does not overlap with the Chandra X-ray position of the ULX, ruling out the possibility that the ULX produced the [Ne V] line), so there is no way to accurately constrain the

 $[\]overline{^{19}}$ The inferred column density, $\log(N_{\rm H}/{\rm cm}^2)=22$, is the minimum possible value using our attenuation curve method and consistent with an unobscured AGN. In this case, $\log(N_{\rm H}/{\rm cm}^2)=22$ should be considered an upper limit to the column density.

 $^{^{20}}$ These error bounds should be considered approximate, as the bounds change during each iterative check in XSPEC with the error command.

Table 3

NuSTAR Flux Upper Limits and Column Density Lower Limits for the AGNs

System	Γ	Observed Flux $(10^{-14} \text{ erg cm}^{-2} \text{ s}^{-1})$			Covering Factor	$\log(N_{\rm H}/{\rm cm}^{-2})$	
(1)	(2)	2–10 keV (3)	3–24 keV (4)	3–10 keV (5)	10–24 keV (6)	(7)	(8)
NGC 4178 NGC 4178 J0851+3926	2.6 2.3 1.8	<8.03 <7.36 <4.84	<6.99 <7.30 <7.47	<5.23 <5.16 <3.77	<7.14 <7.41 <9.40	0.5 0.99 0.5 (0.99)	\$22.0 >24.2 >24.1 (>24.3)

Note. Observed flux upper limits and column density lower limits for the candidate AGNs in NGC 4178 and J0851+3926. Columns (1) and (2): system name and choice of photon index for the modeling. Columns (3)–(6): observed flux upper limits in units of 10^{-14} erg cm⁻² s⁻¹ in the 2–10, 3–24, 3–10, and 10–24 keV energy bands. Column (7): covering factor choice(s) used when inferring column density limits (see Section 3). Column (8): inferred column densities derived from the flux ratios and attenuation curves developed in Section 3. Column densities are rounded to the nearest tenth.

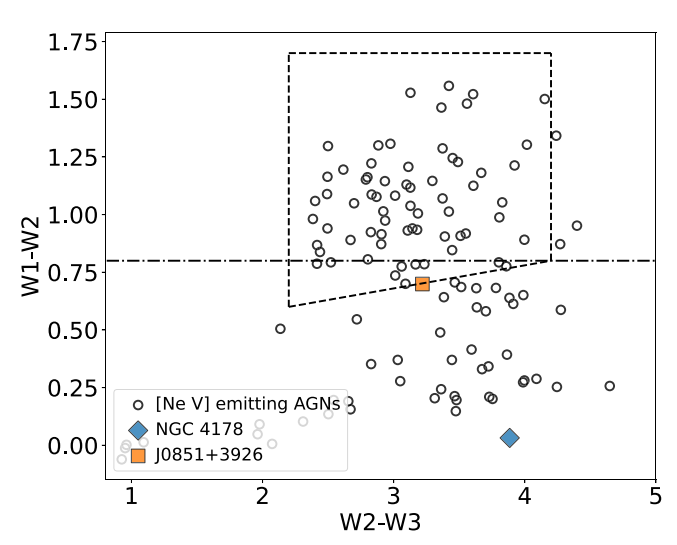


Figure 3. WISE color–color space for [Ne V]-emitting AGNs. The WISE W1–W2 color is given on the y-axis, while the W2–W3 color is given on the x-axis. The horizontal dashed–dotted line at y=0.8 denotes the mid-IR AGN criterion from Stern et al. (2012), while the dashed black wedge is the AGN criterion from Jarrett et al. (2011). The [Ne V]-emitting AGNs are plotted as open circles, while NGC 4178 is plotted with a blue diamond. Like many other [Ne V]-emitting AGNs, NGC 4178 also does not manifest as an AGN in the mid-IR. Object J0851+3926 is also plotted here as an orange square.

location of the [Ne V]-emitting source. However, the detection of this line without a counterpart in the optical or hard X-ray bands suggests the simple explanation that the AGN is currently relatively quiet (possibly an LLAGN) but was more active at some point in the past (Graham et al. 2019). In this case, NGC 4178 may be similar to the fading AGN in Arp 187, which was not detected in the mid-IR (Ichikawa et al. 2016) or the X-rays (Ichikawa et al. 2019a, 2019b), yet a high-ionization [O IV] emission line was marginally-detected in the Spitzer spectra (Ichikawa et al. 2016).

5.2. J0851+3926

As in the case of NGC 4178, while the NuSTAR nondetection in J0851+3926 does not provide confirmation of an AGN or a precise constraint on the potential absorbing column, we can still compare the flux upper limits between observations and derive lower limits to the potential column density. The flux upper limit in the 2–10 keV band derived from NuSTAR, $F_{2-10\text{keV}} < 4.84 \times 10^{-14}$ erg cm⁻² s⁻¹ (see Section 3), which corresponds to a 2–10 keV X-ray luminosity of

 $L_{2-10 {
m keV}}$ < 2.14×10^{42} erg s⁻¹, is an order of magnitude higher than (but consistent with) both the upper limit determined with Chandra in Bohn et al. (2020) and the updated 2–10 keV Chandra upper limit ($L_{2-10 {
m keV}}$ < 2.90×10^{41} erg s⁻¹) derived in Section 3.

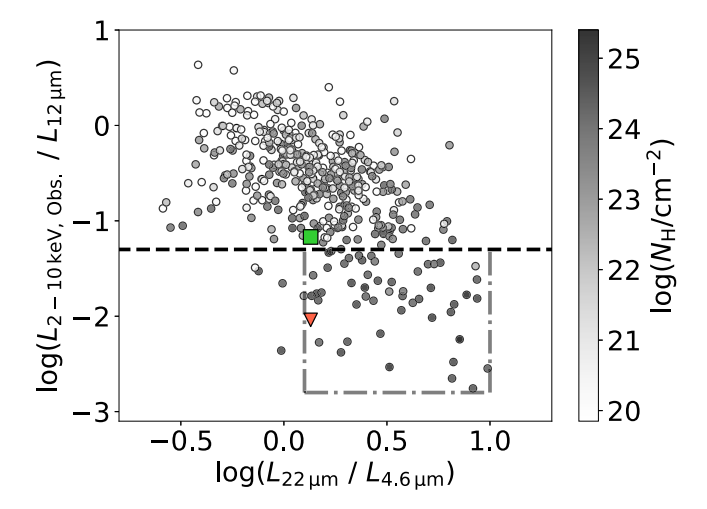
Based on the flux attenuation curves calculated in Section 3, we would expect a nondetection in the NuSTAR 10-24 keV energy band for a column density of $\log(N_{\rm H}/{\rm cm}^2) > 24.1$. This is similar to (albeit slightly smaller than) the column density lower limit calculated in Bohn et al. (2020) using the ratio of the 2–10 keV luminosity and the WISE 12 μ m luminosity (Pfeifle et al. 2022), which was determined to be \sim 24.4 based on the published Chandra upper limit in Bohn et al. (2020). Repeating this latter calculation using the updated 2–10 keV flux upper limit from the Chandra data (Section 4), as well as the 2-10 keV flux upper limit derived from the NuSTAR imaging, we find lower limits to the column density of $\log(N_{\rm H}/{\rm cm}^2) > 24.3$ and 23.9, respectively, when using Expression (2) from Pfeifle et al. (2022) for the column density derived from the ratio $\log(L_{2-10~{\rm keV}}/L_{12~\mu{\rm m}})^{21}$ All three of these calculations yield column densities similar to one another; therefore, we expect this AGN to be at least heavily obscured, if not Compton-thick.

The mid-IR colors of J0851+3926 can offer additional clues to the nature of the source and about the obscuration inherent to the system. It is important to note that J0851+3926 not only meets the stringent three-band color cut defined in Jarrett et al. (2011) but also meets the color cut $W1-W2 \ge 0.7$ (see Figure 3), defined by Stern et al. (2012) as an 85% reliable selection method,²² as well as the 90% reliability criterion of $W1-W2 > 0.662 \times exp\{0.232 \times (W2-13.97)^2\}$ proposed by Assef et al. (2013). Given its selection by three separate and often reliable methods (at least for AGNs hosted by massive galaxies; e.g., Stern et al. 2012), it would be unusual for the mid-IR emission to be driven by other dust heating sources, such as star formation. It is most likely that J0851+3926 does indeed host a heavily obscured AGN that gives rise to both the mid-IR colors of the system and the broad line observed in the near-IR as reported in Bohn et al. (2020), the latter of which is compelling evidence for an AGN in its own right.

Pfeifle et al. (2022) recently published several obscuration diagnostics based on WISE color ratios that we can use here as another means to indirectly probe the column density.

²¹ A slightly revised version of Equations (1) and (2) from Pfeifle et al. (2022) was published following the publication of Bohn et al. (2020), which explains the slight difference in column density.

²² But it does not meet the more commonly used 95% reliable method of W1–W2 > 0.8 (Stern et al. 2012).



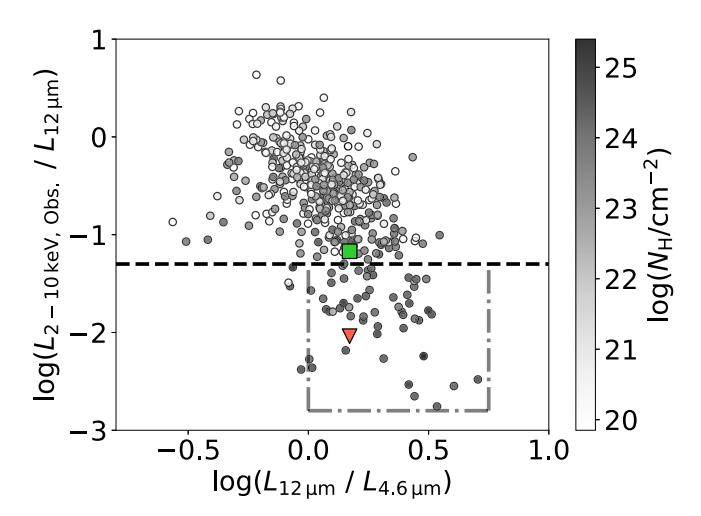


Figure 4. Obscuration diagnostics from Pfeifle et al. (2022) for J0851+3926. It is shown as an inverted red triangle (Chandra) and green square (NuSTAR), while the Swift/BAT AGNs are shown with a gray color map to illustrate how the AGN colors change with column density. The column densities are given on the auxiliary color map. The black dashed line in each panel shows a simple cut of $\log(L_{2-10\text{keV}}/L_{12\mu\text{m}}) < -1.3$ for selecting heavily obscured AGNs, while the black dashed lines in concert with the gray dashed–dotted lines display diagnostic regions developed in Pfeifle et al. (2022). (Top) $\log(L_{22\mu\text{m}}/L_{4.6\mu\text{m}})$ and $\log(L_{2-10\text{keV}}/L_{12\mu\text{m}})$ diagnostic. (Bottom) $\log(L_{12\mu\text{m}}/L_{4.6\mu\text{m}})$ and $\log(L_{2-10\text{keV}}/L_{12\mu\text{m}})$ diagnostic. In both cases, J0851+3926 would be selected as a CT AGN when using the Chandra flux upper limit (red) but just barely misses the cutoff criteria when using the NuSTAR flux upper limit (green).

J0851+3926 exhibits mid-IR colors of $log(L_{12\mu m}/L_{4.6\mu m}) =$ 0.17 and $\log(L_{22\mu\text{m}}/L_{4.6\mu\text{m}}) = 0.13$. Comparing these colors against the obscuration diagnostics presented in Section 3.3 of Pfeifle et al. (2022), J0851+3926 would have been flagged as a Compton-thick (CT) AGN based $\log(L_{22\mu\mathrm{m}}/L_{4.6\mu\mathrm{m}})$ and $\log(L_{12\mu\mathrm{m}}/L_{4.6\mu\mathrm{m}})$ colors. Given that only upper limits on the 2–10 keV flux could be derived using Chandra and NuSTAR, it could have been selected as a candidate CT AGN based on its $\log(L_{2-10 \mathrm{keV}}/L_{12\mu\mathrm{m}})$ ratio; the more stringent 2-10 keV flux upper limit derived from Chandra yields $\log(L_{2-10\text{keV}}/L_{12\mu\text{m}}) < -2.04$, and the upper limit from NuSTAR yields $\log(L_{2-10\text{keV}}/L_{12\mu\text{m}}) < 1.17$. We plot these diagnostic regions in Figure 4 to illustrate this point; J0851 +3926 is represented as a red inverse triangle where the Chandra upper limit is used and as a green square where the NuSTAR upper limit is used, while the gray points indicate the Swift/BAT AGNs color-coded by column density. While this

discussion of mid-IR colors and selection of J0851+3926 is certainly not as quantitative as the column density estimations above, it certainly is in agreement with the scenario in which J0851+3926 hosts a heavily obscured AGN with column density on the order of or in excess of $10^{24} \, \mathrm{cm}^{-2}$.

6. Conclusion

We have presented new NuSTAR observations of two bulgeless galaxies, NGC 4178 and J0851+3926, in an effort to confirm the existence of the heavily buried AGNs reported by Secrest et al. (2012) and Bohn et al. (2020), respectively, and better constrain their column densities. We summarize our results here.

- 1. Neither of the AGNs in NGC 4178 or J0851+3926 are significantly detected by NuSTAR in any of the 3–24, 3–10, or 10–24 keV energy bands.
- 2. There are no hard X-ray-emitting AGNs above an observed 10–24 keV flux limit of 7.41×10^{-14} erg cm $^{-2}$ s $^{-1}$ ($\Gamma=2.3$) in NGC 4178 and 9.40×10^{-14} erg cm $^{-2}$ s $^{-1}$ ($\Gamma=1.8$) in J0851+3926.
- 3. The nondetections with NuSTAR imply column densities of $\log(N_{\rm H}/{\rm cm}^{-2}) > 24.2$ for NGC 4178 (assuming the obscured model with $\Gamma = 2.3$ and C = 0.99 from Secrest et al. 2012) and $\log(N_{\rm H}/{\rm cm}^{-2}) > 24.3$ for J0851+3926 (assuming $\Gamma = 1.8$ and C = 0.99). If the AGN in NGC 4178 is unobscured ($\Gamma = 2.6$; Secrest et al. 2012), its flux is below the detection limit of the NuSTAR observation.
- 4. Comparing our NuSTAR observations to the results of Hebbar et al. (2019), if a supernova is indeed responsible for the observed nuclear X-ray emission in NGC 4178, rather than an AGN, its expected observed X-ray luminosity ($L_{2-10\,\mathrm{keV}}=2.0^{+0.3}_{-0.4}\times10^{-15}$ or $L_{3-10\,\mathrm{keV}}=6.4^{+1.0}_{-1.0}\times10^{-16}\,\mathrm{erg\,cm^{-2}\,s^{-1}}$) is well below the detection limit of our observations.
- 5. Object J0851+3926 is most plausibly a heavily obscured AGN. Object NGC 4178 could be a heavily obscured AGN but is also plausibly an LLAGN with a flux below the detection limit of NuSTAR; the previously detected [Ne V] emission line is likely a light echo, tracing past activity of the intermediate-mass black hole (Graham et al. 2019).

Unfortunately, the NuSTAR observations cannot offer definitive proof of the AGNs in J0851+3926 or NGC 4178, but the upper limits on the fluxes and lower limits on the column densities suggest that future works should focus on near-IR imaging or spectroscopy in order to more easily peer through the presumed high column densities. This is most significantly demonstrated by Bohn et al. (2020), who found clear signatures of the AGN in J0851+3926 based on the detection of a hidden broad-line region while the AGN remains elusive at both optical and (soft and hard) X-ray wavelengths. Infrared observations of these galaxies and other optically elusive AGNs with JWST may offer the most promising avenue for detecting these AGNs via high-excitation coronal line emission and optically hidden broad-line regions.

We would like to thank the anonymous referee for the timely and helpful review that improved the manuscript. We thank George Lansbury for sharing his Python script for calculating Bayesian upper limits. We also thank Kimberly Weaver and Koji Mukai for helpful discussions on using PIMMS for NuSTAR flux estimations.

R.W.P. gratefully acknowledges support from NASA grant 80NSSC21K0063 and through an appointment to the NASA Postdoctoral Program at Goddard Space Flight Center, administered by ORAU through a contract with NASA. C.R. acknowledges support from Fondecyt Iniciacion grant 11190831 and ANID BASAL project FB210003. T.B. and G.C. acknowledge partial support by the National Science Foundation under grant No. AST 1817233. M.R. gratefully acknowledges support from the National Science Foundation Graduate Research Fellowship under grant No. 2141064.

This work makes use of data from the NuSTAR mission, a project led by Caltech, managed by the Jet Propulsion Laboratory, and funded by NASA. We thank the NuSTAR Operations, Software, and Calibration teams for their support with the execution and analysis of these observations. This research has made use of the NuSTAR Data Analysis Software, jointly developed by the ASI Science Data Center (Italy) and Caltech. The scientific results reported in this paper are based in part on data obtained from the Chandra Data Archive and published previously in the cited articles. This research has made use of software provided by the Chandra X-ray Center (CXC) in the application packages CIAO. This work made use of imaging from the Pan-STARRS1 Surveys. This research has made use of the NASA/IPAC Infrared Science Archive, which is funded by the National Aeronautics and Space Administration and operated by the California Institute of Technology. This publication makes use of data products from the Wide-field Infrared Survey Explorer, which is a joint project of the University of California, Los Angeles, and the Jet Propulsion Laboratory/California Institute of Technology, funded by the National Aeronautics and Space Administration. This publication also makes use of data products from NEOWISE, which is a project of the Jet Propulsion Laboratory/California Institute of Technology, funded by the Planetary Science Division of the National Aeronautics and Space Administration.

Facilities: Chandra, NuSTAR, WISE, Pan-STARRS. Software: APLpy (Robitaille & Bressert 2012), pandas (McKinney 2010), NumPy (Harris et al. 2020), SciPy (Virtanen et al. 2020), HEASOFT (Nasa High Energy Astrophysics Science Archive Research Center 2014), MATPLOTLIB (Hunter 2007), XSPEC (Arnaud 1996), PIMMS, CIAO (Fruscione et al. 2006), NUSTARDAS, DS9 (Joye & Mandel 2003).

ORCID iDs

Ryan W. Pfeifle https://orcid.org/0000-0001-8640-8522 Shobita Satyapal https://orcid.org/0000-0003-2277-2354 Claudio Ricci https://orcid.org/0000-0001-5231-2645 Nathan J. Secrest https://orcid.org/0000-0002-4902-8077 Mario Gliozzi https://orcid.org/0000-0002-8818-9009 Thomas Bohn https://orcid.org/0000-0002-4375-254X Gabriela Canalizo https://orcid.org/0000-0003-4693-6157 Michael A. Reefe https://orcid.org/0000-0003-4701-8497

References

```
Abel, N. P., & Satyapal, S. 2008, ApJ, 678, 686
Allen, M. G., Groves, B. A., Dopita, M. A., Sutherland, R. S., & Kewley, L. J. 2008, ApJS, 178, 20
Annuar, A., Alexander, D. M., Gandhi, P., et al. 2020, MNRAS, 497, 229
Arnaud, K. A. 1996, in ASP Conf. Ser. 101, Astronomical Data Analysis Software and Systems V, ed. V. Systems, G. H. Jacoby, & J. Barnes (San Francisco, CA: ASP), 17
```

```
Asmus, D., Gandhi, P., Honig, S. F., Smette, A., & Duschl, W. J. 2015,
  MNRAS, 454, 766
Assef, R. J., Stern, D., Kochanek, C. S., et al. 2013, ApJ, 772, 26
Baldwin, J. A., Phillips, M. M., & Terlevich, R. 1981, PASP, 93, 5
Balokovic, M., Brightman, M., Harrison, F. A., et al. 2018, ApJ, 854, 42
Barnes, J. E. 1992, ApJ, 393, 484
Bell, E. F., Monachesi, A., Harmsen, B., et al. 2017, ApJL, 837, L8
Bohn, T., Canalizo, G., Satyapal, S., & Pfeifle, R. W. 2020, ApJ, 899, 82
Cappi, M., Panessa, F., Bassani, L., et al. 2006, A&A, 446, 459
Cash, W. 1979, ApJ, 228, 939
Cisternas, M., Jahnke, K., Bongiorno, A., et al. 2011, ApJL, 741, L11
de Jong, T., Clegg, P. E., Rowan-Robinson, M., et al. 1984, ApJL, 278, L67
Fruscione, A., McDowell, J. C., Allen, G. E., et al. 2006, Proc. SPIE, 6270,
Gebhardt, K., Bender, R., Bower, G., et al. 2000, ApJL, 539, L13
Graham, A. W., Soria, R., & Davis, B. L. 2019, MNRAS, 484, 814
Gültekin, K., Cackett, E. M., Miller, J. M., et al. 2009a, ApJ, 706, 404
Gültekin, K., Richstone, D. O., Gebhardt, K., et al. 2009b, ApJ, 698, 198
Harris, C. R., Millman, K. J., van der Walt, S. J., et al. 2020, Natur, 585,
Harrison, F. A., Craig, W. W., Christensen, F. E., et al. 2013, ApJ, 770, 103
Hebbar, P. R., Heinke, C. O., Sivakoff, G. R., & Shaw, A. W. 2019, MNRAS,
  485, 5604
Ho, L. C., Filippenko, A. V., & Sargent, W. L. W. 1997, ApJ, 487, 568
Hopkins, P. F., Cox, T. J., Younger, J. D., & Hernquist, L. 2009, ApJ,
   691, 1168
Hopkins, P. F., Keres, D., Murray, N., Quataert, E., & Hernquist, L. 2012,
   MNRAS, 427, 968
Hunter, J. D. 2007, CSE, 9, 90
Ichikawa, K., Kawamuro, T., Shidatsu, M., et al. 2019a, ApJL, 883, L13
Ichikawa, K., Ueda, J., Bae, H.-J., et al. 2019b, ApJ, 870, 65
Ichikawa, K., Ueda, J., Shidatsu, M., Kawamuro, T., & Matsuoka, K. 2016,
  PASJ, 68, 9
Jarrett, T. H., Cohen, M., Masci, F., et al. 2011, ApJ, 735, 112
Joye, W. A., & Mandel, E. 2003, in ASP Conf. Ser. 295, Astronomical Data
   Analysis Software and Systems XII, ed. X. I. I. Systems, H. E. Payne,
   R. I. Jedrzejewski, & R. N. Hook (San Francisco, CA: ASP), 489
Kauffmann, G., & Haehnelt, M. 2000, MNRAS, 311, 576
Kauffmann, G., Heckman, T. M., Tremonti, C., et al. 2003, MNRAS,
   346, 1055
Kent, B. R., Giovanelli, R., Haynes, M. P., et al. 2008, AJ, 136, 713
Kewley, L. J., Dopita, M. A., Sutherland, R. S., Heisler, C. A., & Trevena, J.
  2001, ApJ, 556, 121
Kewley, L. J., Groves, B., Kauffmann, G., & Heckman, T. 2006, MNRAS,
  372, 961
Kocevski, D. D., Faber, S. M., Mozena, M., et al. 2012, ApJ, 744, 148
Kraft, R. P., Burrows, D. N., & Nousek, J. A. 1991, ApJ, 374, 344
Lansbury, G. B., Alexander, D. M., Moro, A. D., et al. 2014, ApJ, 785, 17
Lansbury, G. B., Stern, D., Aird, J., et al. 2017, ApJ, 836, 99
Magorrian, J., Tremaine, S., Richstone, D., et al. 1998, AJ, 115, 2285
Martig, M., Bournaud, F., Croton, D. J., Dekel, A., & Teyssier, R. 2012, ApJ,
   756, 26
McConnell, N. J., & Ma, C.-P. 2013, ApJ, 764, 184
McKinney, W. 2010, in Proc. of the 9th Python in Science Conf., ed.
   S. van der Walt & J. Millman, 56
Mushotzky, R. F., Done, C., & Pounds, K. A. 1993, ARA&A, 31, 717
Nasa High Energy Astrophysics Science Archive Research Center 2014,
   HEAsoft: Unified Release of FTOOLS and XANADU, Astrophysics Source
   Code Library, ascl:1408.004
NEOWISE Team 2020, NEOWISE-R Single Exposure (L1b) Source
   Table, IPAC
Perri, M., Puccetti, S., Spagnuolo, N., et al. 2021, The NuSTAR Data Analysis
   Software Guide, v1.9.7, ASI Space Science Data Center and California
   Institute of Technology
Pfeifle, R. W., Ricci, C., Boorman, P. G., et al. 2022, ApJS, 261, 3
Ricci, C., Ueda, Y., Koss, M. J., et al. 2015, ApJL, 815, L13
Ricci, C., Trakhtenbrot, B., Koss, M. J., et al. 2017, ApJS, 233, 17
Rich, J. A., Kewley, L. J., & Dopita, M. A. 2011, ApJ, 734, 87
Rich, J. A., Kewley, L. J., & Dopita, M. A. 2014, ApJL, 781, L12
Robitaille, T., & Bressert, E. 2012, APLpy: Astronomical Plotting Library in
  Python, Astrophysics Source Code Library, record, ascl:1208.017
Satyapal, S., Boker, T., Mcalpine, W., et al. 2009, ApJ, 704, 439
Satyapal, S., Secrest, N. J., McAlpine, W., et al. 2014, ApJ, 784, 113
Secrest, N. J., Satyapal, S., Gliozzi, M., et al. 2012, ApJ, 753, 38
Silk, J., & Rees, M. J. 1998, A&A, 331, L1
Simmons, B. D., Smethurst, R. J., & Lintott, C. 2017, MNRAS, 470, 1559
```

Simmons, B. D., Urry, C. M., Schawinski, K., Cardamone, C., & Glikman, E. 2012, ApJ, 761, 75

Springel, V., & Hernquist, L. 2005, ApJL, 622, L9

Stern, D., Assef, R. J., Benford, D. J., et al. 2012, ApJ, 753, 30

Toomre, A. 1977, in Proc. Conf. at Yale Univ., Evolution of Galaxies and Stellar Populations, ed. B. M. Tinsley & R. B. Larson (New Haven, CT: Yale Univ. Obs.), 401

Trump, J. R., Sun, M., Zeimann, G. R., et al. 2015, ApJ, 811, 26
Ueda, Y., Eguchi, S., Terashima, Y., et al. 2007, ApJL, 664, L79
Virtanen, P., Gommers, R., Oliphant, T. E., et al. 2020, NatMe, 17, 261
Willingale, R., Starling, R. L. C., Beardmore, A. P., Tanvir, N. R., & O'Brien, P. T. 2013, MNRAS, 431, 394
Wright, E. L., Eisenhardt, P. R. M., Mainzer, A. K., et al. 2019, AllWISE Source Catalog, IPAC, doi:10.26131/IRSA1